Dislocation decorrelation and relationship to deformation microtwins during creep of a γ′ precipitate strengthened Ni-based superalloy

R.R. Unocic [a,b,*], N. Zhou [b], L. Kovarik [b,c], C. Shen [d], Y. Wang [b], M.J. Mills [b]

[a] *Materials Science and Technology Division, Oak Ridge National Laboratory, Oak Ridge, TN 37831, USA*
[b] *Department of Materials Science and Engineering, The Ohio State University, Columbus, OH 43210, USA*
[c] *EMSL, Pacific Northwest National Laboratory, Richland, WA 99352, USA*
[d] *GE Global Research, Niskayuna, NY 12309, USA*

Abstract

The evolution of microtwins during high temperature creep deformation in a γ′ strengthened Ni-based superalloy has been investigated through a combination of creep testing, transmission electron microscopy (TEM), theoretical modeling, and computer simulation. Experimentally, microtwin nucleation sources were identified and their evolution was tracked by characterizing the deformation substructure at different stages of creep deformation. Deformation is highly localized around stress concentrators such as carbides, borides and serrated grain boundaries, which act as sources of $a/2\langle 110\rangle$ matrix-type dislocations. Due to fine channels between the γ′ particles, coupled with a low γ matrix stacking fault energy, the $a/2\langle 110\rangle$ matrix dislocations dissociate into $a/6\langle 112\rangle$ Shockley partials, which were commonly observed to be decorrelated from one another, creating extended intrinsic stacking faults in the γ matrix. Microtwins are common and form via Shockley partial dislocations, cooperatively shearing both the γ and γ′ phases on adjacent {1 1 1} glide planes. The TEM observations lead directly to an analysis of dislocation–precipitate interactions. The important processes of dislocation dissociation and decorrelation were modeled in detail through phase field simulations and theoretical analyses based on Orowan looping, providing a comprehensive insight into the microstructural features and applied stress conditions that favor the microtwinning deformation mode in γ′ strengthened Ni-based superalloys.
Published by Elsevier Ltd. on behalf of Acta Materialia Inc.

Keywords: Creep; Microtwinning; Shockley partial dislocations; Diffusion; Atomic ordering

1. Introduction

Ni-based superalloys are a class of alloys that are predominantly used in the aerospace industry in hot sections of gas turbine engine components. These alloys possess an attractive combination of attributes, such as high temperature mechanical properties (strength, creep, and fatigue) and resistance to high temperature oxidation. The high temperature mechanical properties are largely dictated by the presence of ordered, L1$_2$ structured, Ni$_3$Al-based γ′

precipitates, which are coherently embedded in a solid solution γ matrix (fcc structure). Since these materials are utilized at elevated temperatures, time-dependent creep deformation is of principal concern. There have been numerous detailed transmission electron microscopy (TEM) studies focused on elucidating the creep deformation mechanisms and determining the associated implications for creep rate controlling dislocation processes [1–8]. Mechanisms previously identified include dislocation climb, looping, and stacking fault related γ′ shearing. A particular mechanism that has been reported more recently following high temperature creep deformation is microtwinning [9–17], which is surprising since twinning in fcc crystals is generally considered a low temperature, high

---

* Corresponding author at: Materials Science and Technology Division, Oak Ridge National Laboratory, Oak Ridge, TN 37831, USA. Tel.: +1 865 574 0096.

E-mail address: unocicrr@ornl.gov (R.R. Unocic).

Report Documentation Page

1. REPORT DATE **JUL 2011**	2. REPORT TYPE	3. DATES COVERED **00-00-2011 to 00-00-2011**

4. TITLE AND SUBTITLE **Dislocation decorrelation and relationship to deformation microtwins during creep of a Y' precipitate strengthened Ni-based superalloy**	5a. CONTRACT NUMBER
	5b. GRANT NUMBER
	5c. PROGRAM ELEMENT NUMBER
6. AUTHOR(S)	5d. PROJECT NUMBER
	5e. TASK NUMBER
	5f. WORK UNIT NUMBER

7. PERFORMING ORGANIZATION NAME(S) AND ADDRESS(ES) **Oak Ridge National Laboratory,Materials Science and Technology Division,Oak Ridge,TN,37831**	8. PERFORMING ORGANIZATION REPORT NUMBER

9. SPONSORING/MONITORING AGENCY NAME(S) AND ADDRESS(ES)	10. SPONSOR/MONITOR'S ACRONYM(S)
	11. SPONSOR/MONITOR'S REPORT NUMBER(S)

12. DISTRIBUTION/AVAILABILITY STATEMENT
Approved for public release; distribution unlimited

13. SUPPLEMENTARY NOTES

14. ABSTRACT
The evolution of microtwins during high temperature creep deformation in a c0 strengthened Ni-based superalloy has been investigated through a combination of creep testing, transmission electron microscopy (TEM), theoretical modeling, and computer simulation. Experimentally, microtwin nucleation sources were identified and their evolution was tracked by characterizing the deformation substructure at different stages of creep deformation. Deformation is highly localized around stress concentrators such as carbides, borides and serrated grain boundaries, which act as sources of a/2h110i matrix-type dislocations. Due to fine channels between the c0 particles coupled with a low c matrix stacking fault energy, the a/2h110i matrix dislocations dissociate into a/6h112i Shockley partials, which were commonly observed to be decorrelated from one another, creating extended intrinsic stacking faults in the c matrix. Microtwins are common and form via Shockley partial dislocations, cooperatively shearing both the c and c0 phases on adjacent {11 1} glide planes. The TEM observations lead directly to an analysis of dislocation?precipitate interactions. The important processes of dislocation dissociation and decorrelation were modeled in detail through phase field simulations and theoretical analyses based on Orowan looping, providing a comprehensive insight into the microstructural features and applied stress conditions that favor the microtwinning deformation mode in c0 strengthened Ni-based superalloys.

15. SUBJECT TERMS

16. SECURITY CLASSIFICATION OF:			17. LIMITATION OF ABSTRACT	18. NUMBER OF PAGES	19a. NAME OF RESPONSIBLE PERSON
a. REPORT **unclassified**	b. ABSTRACT **unclassified**	c. THIS PAGE **unclassified**	**Same as Report (SAR)**	**15**	

strain rate deformation mode, in contrast to the high temperature, low strain rate creep conditions that have been observed in these alloys [18].

As with many dislocation-based deformation mechanisms commonly observed in γ' strengthened Ni-based superalloys, dislocation–precipitate interactions are highly dependent upon alloy chemistry, γ' precipitate size and morphology, γ channel width, crystal orientation, stress and temperature. The crystallographic orientation stress dependence of microtwinning in a single crystal SRR99 superalloy was shown by Ardakani et al. [10], where it was determined that activation of $\{1\,1\,1\}\langle 1\,1\,2\rangle$ and $\{1\,1\,1\}\langle 1\,1\,0\rangle$ slip systems occurs when the tensile stress axis is aligned with, or rotated towards, the [0 1 1] and [1 1 1] crystallographic directions. Similarly, uniaxial creep experiments of single crystal CMSX-4 by Knowles et al. [11,12] reported in greater detail how the activation of $\{1\,1\,1\}\langle 1\,1\,2\rangle$ slip systems can initiate both stacking fault shear and twinning. It was suggested that microtwins form by the motion of $a/3\langle 1\,1\,2\rangle$-type superlattice Shockley partials on adjacent $\{1\,1\,1\}$ glide planes since the L1$_2$ structure of the γ' precipitates would be preserved, as shown in Fig. 1a. However, this would effectively require high stresses for such a large displacement.

According to Christian and Mahajan [19] deformation-induced twinning in L1$_2$ superlattice structures would result in the production of a pseudotwin characterized by an imperfect superlattice with incorrect atomic ordering if sheared by $a/6\langle 1\,1\,2\rangle$ Shockley partial dislocations, as illustrated in Fig. 1b. Atomic rearrangement would thus be required to convert the pseudotwin structure to a true twin structure with the correct nearest neighbor atomic bonds. Accordingly, Kolbe proposed a hypothesis whereby

microtwins in γ' strengthened superalloys form by the pairwise passage of identical $a/6\langle 1\,1\,2\rangle$ Shockley partial dislocations that shear through both γ and γ' on adjacent $\{1\,1\,1\}$ glide planes [20]. Considering the fact that shearing of the γ' precipitates by a single Shockley partial dislocation would form a high energy, complex stacking fault (CSF), and passage of a second $a/6\langle 1\,1\,2\rangle$ Shockley partial would create a two layer CSF, Kolbe proposed that diffusion-mediated atomic reordering in the wake of the leading partial could convert the two layer CSF into a superlattice extrinsic stacking fault (SESF) by local rearrangement of atoms to eliminate the high energy Al–Al first nearest neighbor bonds. Although direct TEM evidence was not provided at the time, it was later substantiated through direct TEM observations that microtwins actually formed when both the γ matrix and γ' precipitates were sheared conservatively by identical, paired $a/6\langle 1\,1\,2\rangle$ Shockley partial dislocations traveling on adjacent $\{1\,1\,1\}$ type octahedral glide planes [14,15].

In a more recent study the concept of reorder-mediated shearing of γ' precipitates was conclusively identified as playing a role in microtwin formation in Ni-based superalloys [14], and a quantitative model for the creep rate for microtwinning was proposed [21]. The energetics associated with the reordering process was explored using first principles calculations [22] where the most likely diffusional paths were identified. This analysis suggests that the activation energy barrier for reordering should be very similar to that for Ni self-diffusion in the ordered phase, under the simplifying assumption of Ni$_3$Al being representative of the γ' structure. In addition to controlling the rate of thermally activated microtwinning, it has been postulated that reorder-mediated shearing may also be rate limiting to the
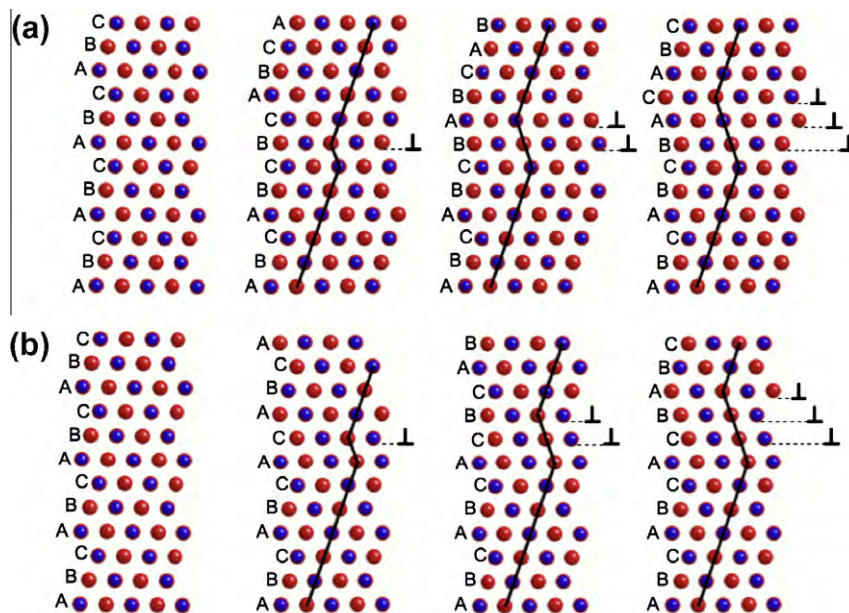

Fig. 1. Schematic illustration of twinning in the L1$_2$ structure of the γ' precipitate phase. (a) Creation of a true twin structure by passage of $a/3\langle 1\,1\,2\rangle$ super Shockley partial dislocations on adjacent $\{1\,1\,1\}$ planes; (b) creation of a pseudotwin structure of $a/6\langle 1\,1\,2\rangle$ Shockley partial dislocations on adjacent $\{1\,1\,1\}$ planes.

formation of both superlattice intrinsic and extrinsic stacking faults in superalloys at elevated temperatures [22]. Based on the concept of the generalized stacking fault energy landscape, phase field modeling has been used to parametrically study microstructural effects on the critically resolved shear stress, which was also coupled with temperature effects on the atomic reordering kinetics related to dislocation glide [23]. The aforementioned rate limiting process helps explain the dynamic motion of twinning partial dislocations and microtwin propagation captured by Legros et al. [17] during elevated temperature *in situ* TEM straining experiments of a rafted γ/γ' superalloy, where it was observed that the twinning partial dislocations moved at a higher velocity in the γ phase and a lower velocity in the γ' phase.

Recent research on creep deformation mechanisms in polycrystalline Ni-based turbine disk superalloy Rene 104 has shown that microtwinning is a dominant deformation mechanism during creep at a test temperature of 677 °C and a stress level of 690 MPa [16]. Deformation in this case was carried out to such a high level of plastic deformation (2.0% strain) that it was difficult to capture discrete locations where microtwins may have initiated or terminated. Due to the present lack of experimental evidence on microtwin initiation and evolution there has yet to be a detailed description of how the microstructure and other external variables (stress and temperature) dictate the microtwinning process from initiation to propagation. Therefore, the motivation for this study was to perform an in-depth experimental, theoretical, and computational study on the evolution of the microtwinning deformation mode by focusing on the salient microstructural features that promote microtwinning over other deformation mechanisms.

2. Materials and experimental procedure

The material used in this study is a powder metallurgy product, polycrystalline Ni-based turbine disk alloy (Rene 104) that was supplied in the form of a scaled up turbine disk forging by General Electric Aircraft Engines (GEAE, Evendale, OH). The nominal composition of this alloy, which has Co, Cr, Al and Ti as the major alloying elements, is given elsewhere [24]. The disk forging was subjected to a proprietary two step supersolvus heat treatment, which refers to a final heat treatment wherein the primary γ' precipitates that are present during the powder compaction, extrusion, and forging processes, are re-solutionized back into the matrix, then precipitated as a multimodal γ' precipitate size distribution [25,26]. For the material in this study the resulting microstructure consisted of a bimodal size distribution of γ' precipitates, with the coarser being the secondary γ' and finer being the tertiary γ' precipitates. On average the secondary and tertiary γ' precipitate sizes (and volume fractions) were experimentally measured to be 186.6 (48.4%) and 25.5 nm (2.7%), respectively, using quantitative image analysis on material that was
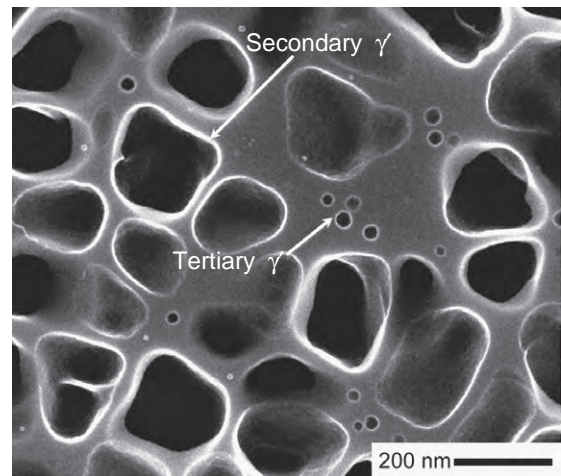

Fig. 2. Microstructure of Ni-based disk superalloy Rene 104 following a supersolvus heat treatment. SEM image shows the bimodal γ' precipitate size distribution (average secondary and tertiary γ' precipitate sizes 186 and 25 nm, respectively).

extracted from the rim section of the turbine disk forging (Fig. 2). Specimens for creep testing and TEM deformation mechanism identification were extracted by wire electric discharge machining (EDM) from the same location and prepared as standard round tensile creep specimens.

In order to track the evolution of the microtwins and to determine the salient microstructural features that give rise to microtwinning the tests were interrupted at varying stages of creep deformation. Constant load tensile creep experiments were preformed at 677 °C and 724 MPa and interrupted at nominally 0.05%, 0.2%, and 1.0% strain. Specimens were cooled under load to preserve the deformation substructure. Following creep testing thin foils for TEM substructure characterization studies were extracted from the gage at a 45° angle with respect to the tensile axis in order to maximize the probability of imaging deformation activity along slip planes that experienced maximum shear stress. The foils were mechanically thinned using progressively finer SiC paper to a thickness of 150 μm then slurry drilled. Final thinning was performed in a Struers Tenupol 5 twin jet polishing unit using an electrolyte consisting of 60% methanol, 35% 2-n-butoxyethanol, and 5% perchloric acid at a temperature of –45 °C and applied voltage of 15 V. A detailed diffraction contrast TEM analysis was performed using a Philips CM200 or a FEI Tecnai TF20 microscope, operated at 200 keV. High resolution TEM (HRTEM) and high angle annular dark field (HAADF) imaging were performed in a probe-corrected FEI Titan field emission gun transmission electron microscope operated at 300 keV.

3. Results

3.1. Microtwinning as the dominant deformation process at larger strain

Following creep at 677 °C to 0.98% plastic strain over 2725 h microtwinning was found to be the dominant mode of deformation. Fig. 3a and b shows a bright field (BF) TEM image of the microtwins (viewed nearly edge on and oriented along the [011] zone axis) and the corresponding selected area diffraction (SAD) pattern, respectively. The SAD pattern shows fundamental reflections from the γ matrix, superlattice reflections from the γ′ precipitates, and the {111} twin reflections, confirming that the planar defects are microtwins. Further support is provided by the HRTEM images shown in Fig. 4, where twins of several different thicknesses are shown which can be as narrow as two {111} planes (Fig. 4a) or as thick as several

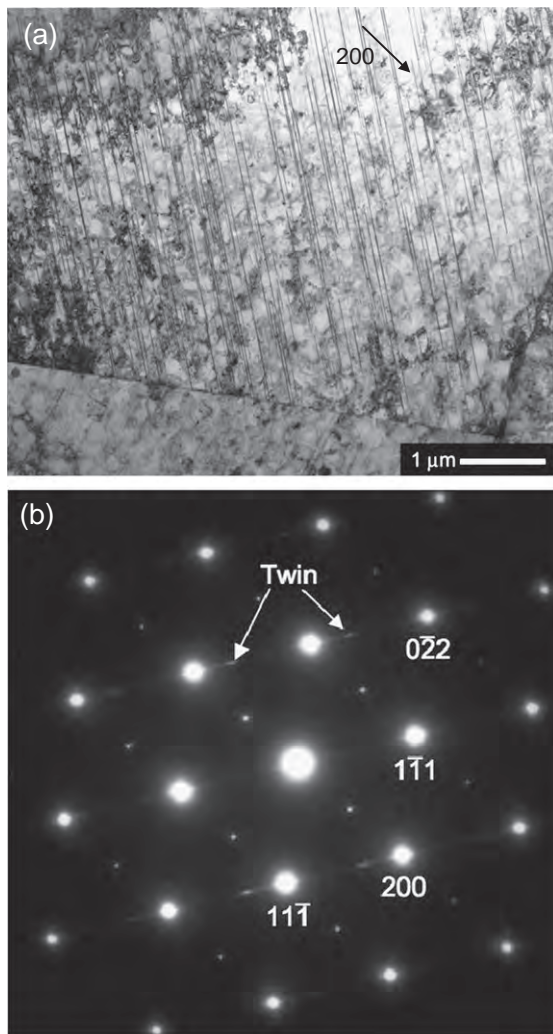Fig. 4. HRTEM images of microtwins present within the γ matrix phase at different thicknesses.

Fig. 3. (a) BF TEM micrograph of microtwins formed during creep deformation to 0.98% strain at 677 °C and 724 MPa. (b) SAD pattern showing the fundamental γ matrix, γ′ precipitate superlattice, and twin reflections (marked by arrows). *B* = [011].
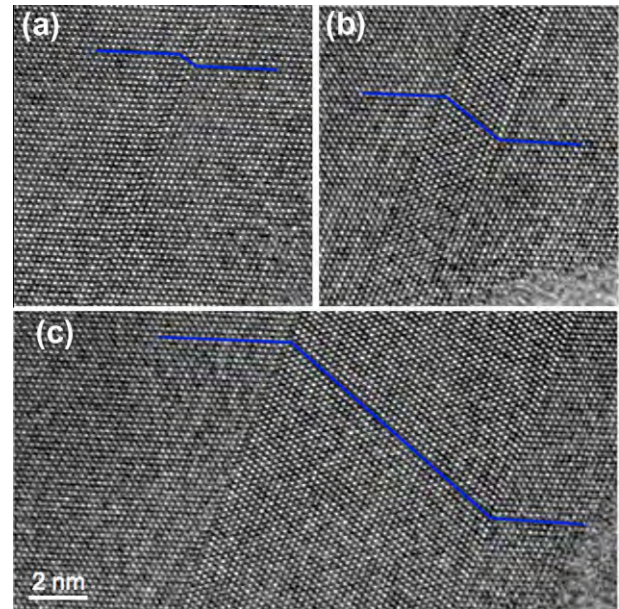
tens of atomic planes (Fig. 4b and c). The two layer fault structure is recognized as an extrinsic stacking fault in the matrix and as a superlattice extrinsic stacking fault in the precipitates [22,27].

Although the $a/3\langle112\rangle$ partial is recognized to be the twinning partial in the γ′ phase [19], extensive investigations using conventional diffraction contrast imaging [14] and HAADF scanning transmission electron microscopy (STEM) imaging [22] has shown that microtwins propagate by the motion of identical $a/6\langle112\rangle$ Shockley partial dislocations that shear through both the γ matrix and γ′ precipitates on adjacent {111} glide planes, an example of which is shown in Fig. 5. As mentioned previously and discussed in detail elsewhere [22], shearing of the precipitates is believed to be thermally activated due to diffusion-mediated reordering of the high energy faults that would be created in the wake of the Shockley partials. We now focus on the processes that occur during the earlier stages of creep deformation that ultimately lead to this microtwinned substructure.

3.2. Initiation of microtwins

In order to identify the nucleation sources of the microtwins it was necessary to examine the deformation substructure at the earliest stages of deformation. TEM examination following 0.05% plastic strain revealed a particular grain of interest, which allowed a unique view of the deformation activity, as viewed down the (111) glide plane. A low magnification BF STEM image of this particular grain is shown in Fig. 6. The grain was bounded by typical high angle, serrated grain boundaries, as well as an annealing twin boundary, which is observed on the lower edge of
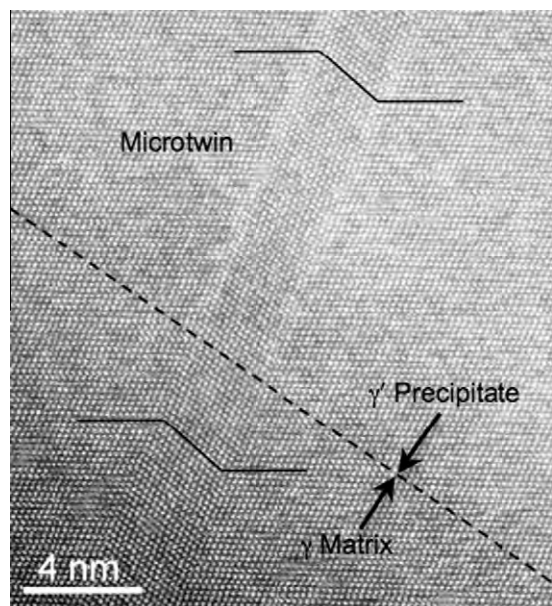
Fig. 5. Representative HAADF STEM image of microtwin shearing through both the γ matrix and γ′ precipitate.
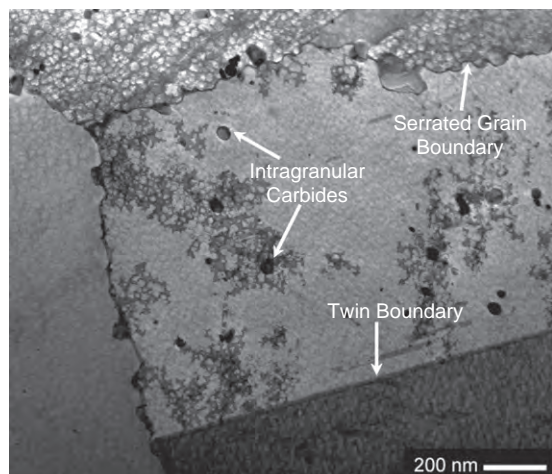

Fig. 6. BF STEM image of the deformation substructure following creep to 0.05% strain at 677 °C and 724 MPa showing deformation activity being emitted from second phase particles and grain boundaries.

the image. A number of carbide and/or boride phases are present, both along grain boundaries and within the grain interiors. These second phase particles are typically found in this and other polycrystalline superalloys produced by powder metallurgical processes [28]. For instance, the chemical composition of the intragranular particles as determined by energy dispersive X-ray spectroscopy tended to be enriched in Ti, Ta, Co, Cr, Mo, and Nb, indicating a MC type carbide [29]. Both $M_{23}C_6$ carbides, enriched in Co, Cr, Mo, C and B, as well as borides, have also been observed along grain boundaries. Upon closer examination these minor carbide and boride phases appear to be distinct origins of deformation activity. The nascent deformation activities near these second phases are in the form of both

dislocations and stacking faults in the matrix. Note that the stacking faults viewed in this orientation, with the fault plane nearly parallel to the foil plane, do not show the alternating bright and dark fringes normally expected when characterizing stacking faults. Instead, the stacking faults appear as dark grey regions and are present within the γ matrix.

3.3. Detailed TEM deformation substructure analysis

Additional diffraction contrast TEM analysis was required to confirm that dislocations emitted from the grain boundary carbides/borides or intragranular carbide sources readily dissociate into Shockley partial dislocations. Fig. 7 presents a series of higher magnification BF TEM images (using different two beam diffraction conditions) of the defect structures near one of the intragranular carbides shown in Fig. 6. The specific dislocation configuration highlighted in the schematic illustration of Fig. 7f indicates that the leading partial dislocation has "percolated" between the secondary γ′ precipitates, leaving them unsheared, while some of the finer scale tertiary γ′ precipitates have been looped by the leading partial. The stacking fault and associated Shockley partial dislocations were determined to be on the (1 1 1) glide plane (which is close to the foil normal in this grain) based on the $g \cdot \mathbf{R}$ invisibility criterion for planar faults in the fcc crystal structure, where $\mathbf{R}$ is the fault vector. The stacking fault is visible in Fig. 7a since $g = \bar{1}11$ and $g \cdot \mathbf{R}$ is not zero. For this case the leading partial dislocation is visible but the trailing one is not. Conversely, using $g = 1\bar{1}1$ (Fig. 7b) the trailing dislocation is visible while the leading one is not. Additional g vectors were chosen such that $g \cdot \mathbf{R} = 0$ and the contrast due to the partial dislocations was not obscured by the stacking fault. For instance, the trailing partial dislocation is visible for $g = \bar{2}20$ (Fig. 7c) and $g = 02\bar{2}$ (Fig. 7d), while it is invisible when imaged with $g = 20\bar{2}$ (Fig. 7e). The leading partial dislocation is visible when imaged with $g = \bar{2}20$ and $g = 20\bar{2}$, while it is invisible with $g = 02\bar{2}$. Based on this analysis, the leading partial dislocation has a Burgers vector of $a/6[\bar{2}\,1\,1]$ and the trailing partial dislocation has a Burgers vector of $a/6[\bar{1}\,2\,\bar{1}]$, produced by the dissociation of a perfect $a/2[\bar{1}\,1\,0]$ matrix dislocation. For a clearer illustration of this dislocation configuration a schematic is presented in Fig. 7f with regard to the (1 1 1) plane of the Thompson's tetrahedron. In addition to determining the Burgers vectors of the dislocations, it is also evident that a single slip system was operative in this region, since all the dislocations can be accounted for by contrast from these perfect and Shockley partial dislocations.

With increasing creep deformation to 0.2% strain the same stacking faults are observed; however, they are present at a much higher density. The local plastic zone near an intragranular carbide is shown at a higher TEM magnification in Fig. 8, which shows several $a/2\langle110\rangle$ dislocations originating from an intragranular carbide source. In this
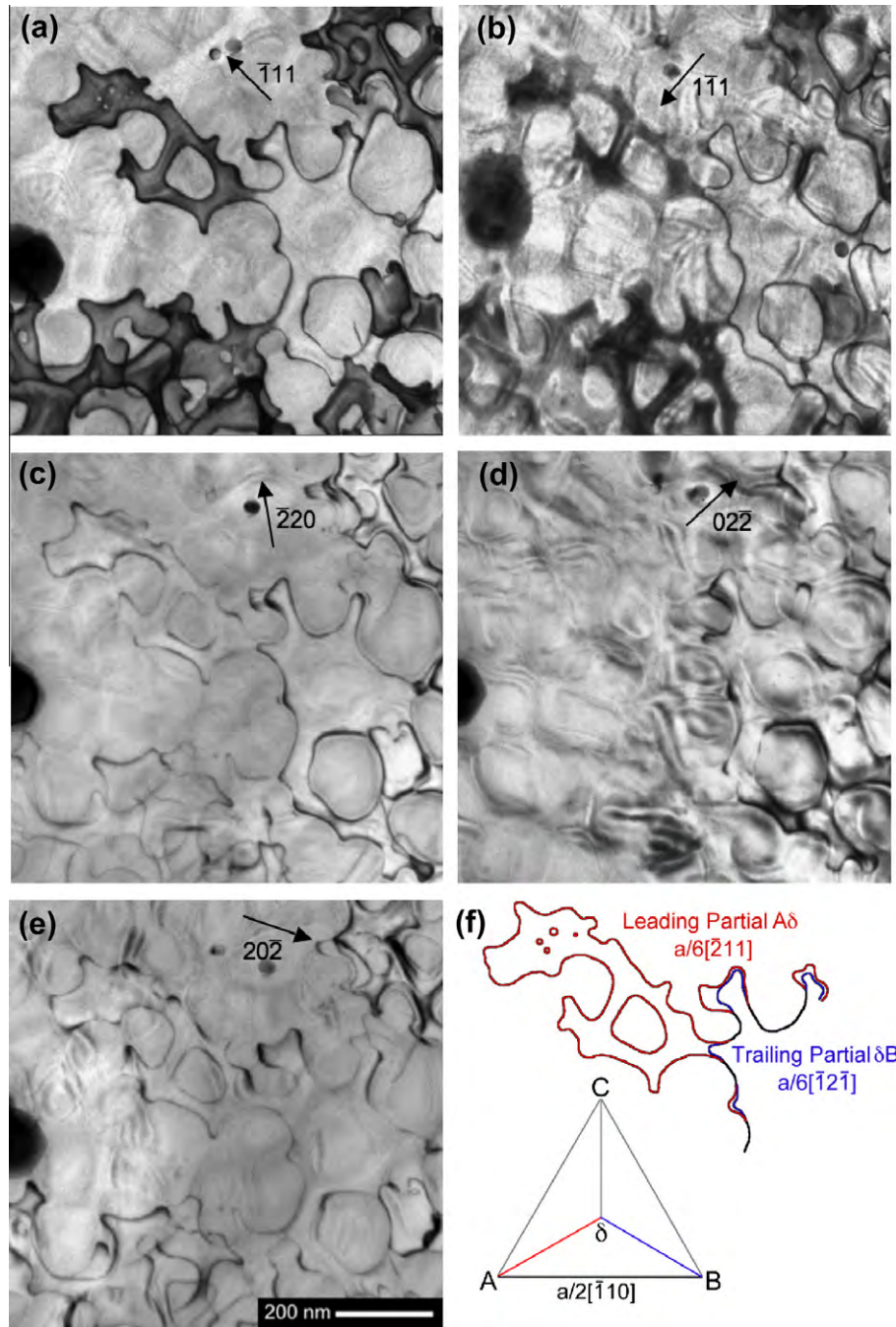
Fig. 7. A series of BF TEM images showing the diffraction contrast analysis of perfect and partial dislocations bounding a stacking fault in the γ matrix using the following imaging conditions: (a) $g = \bar{1}11$, $B = [2\,1\,1]$; (b) $g = 1\bar{1}1$, $B = [1\,1\,0]$; (c) $g = \bar{2}20$, $B = [1\,1\,1]$; (d) $g = 02\bar{2}$, $B = [1\,1\,1]$; (e) $g = 20\bar{2}$, $B = [1\,1\,1]$. (f) Schematic illustration of the dislocation configurations along with Thompson tetrahedron notation of the Burgers vector.

case dislocation emissions on inclined {1 1 1} glide planes are observed. The dislocations directly adjacent to the carbide are comprised predominantly of narrowly dissociated $a/2\langle110\rangle$ dislocations, all contained within the γ matrix. There are also a few instances where significantly wider dissociation events occurred, creating wide stacking faults (labeled F in Fig. 8a). Fig. 8b shows the defect structure a few hundred nanometers from the same carbide, exhibiting primarily stacking faults in the matrix, with Shockley partials looping the secondary γ' precipitates. Thus, these

observations suggest that while $a/2\langle110\rangle$ dislocations are initially generated near carbides, a progression towards a fully dissociated (decorrelated) condition occurs, where the Shockley partials comprising the $a/2\langle110\rangle$ dislocations are widely separated.

It is important to note that these stacking fault structures appear to be present at a similar density to that observed for microtwins formed at larger strain, which further confirms the importance of the former as a precursor to microtwinning. In addition, nearly all of the grains
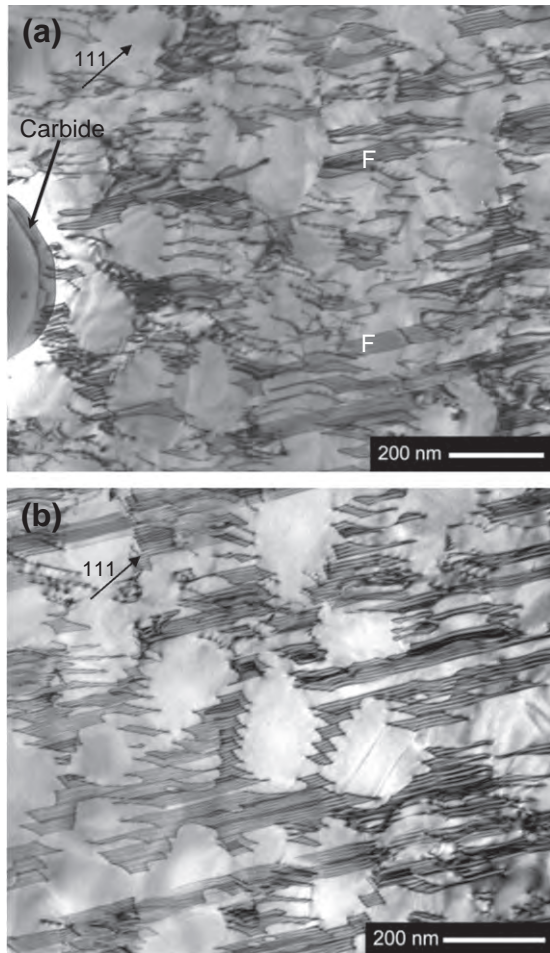
Fig. 8. BF TEM images of (a) the plastic zone surrounding an intragranular carbide, showing emission of dissociated glide $a/2\langle 110\rangle$ dislocations, with a few dissociated into wider stacking faults (marked F) and (b) widely dissociated $a/2\langle 110\rangle$ dislocations in a region approximately 1 μm from the carbide.
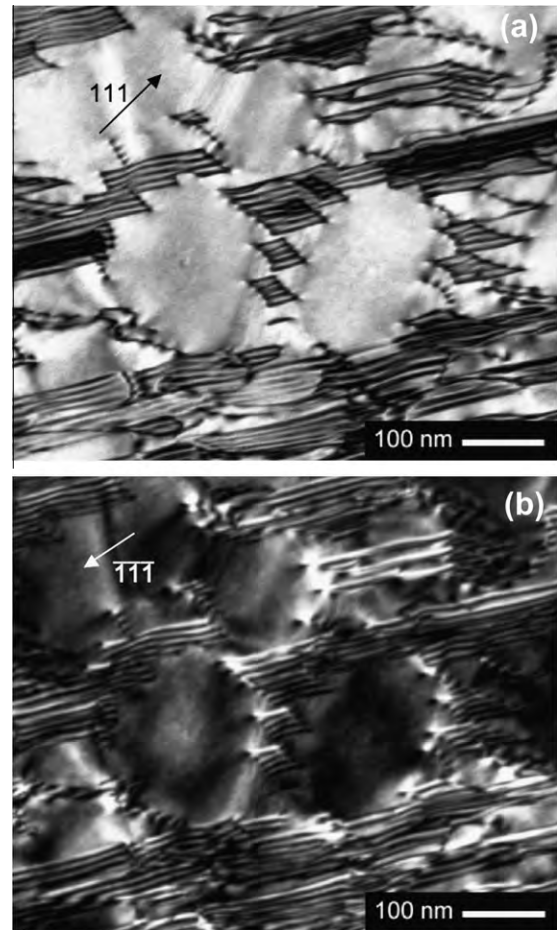

Fig. 9. (a) BF TEM and (b) centered DF TEM images of stacking faults in the γ matrix developed during creep deformation to 0.2% strain at 677 °C and 724 MPa.

examined via TEM possess these deformation features. When the faults are either inclined or nearly edge on with respect to the foil normal, it is observed that a majority of the faults do not shear through the γ′ precipitates. As mentioned in the previous section, this indicates that the decorrelated Shockley partial dislocations bounding the stacking faults do not shear through the precipitates themselves, since this would leave a complex stacking fault. Instead, the $a/6\langle 112\rangle$ Shockley partial dislocation loops that are left around the precipitates have the same Burgers vector as the leading Shockley partial dislocation, and an intrinsic stacking fault is left within the matrix.

The nature of the stacking faults at 0.2% creep strain were determined through complementary BF/DF TEM imaging pairs under a two beam diffraction condition with the deviation parameter set close to $s = 0$ and the operative diffraction vector $g = 111$ and $g = \bar{1}\bar{1}\bar{1}$. As seen in Fig. 9a and b, the outer fringes in the BF image are symmetrical and the outer fringes in the centered DF image are asymmetrical. Several of the stacking faults overlap in this

image, so this analysis is focused on the three stacking faults between the two secondary γ′ precipitates in the center of the image in Fig. 9. To determine whether the stacking faults are intrinsic or extrinsic in nature the g vector is placed in the center of the stacking fault in the centered DF image (Fig. 9b). Under these imaging conditions the g vector points away from the bright outer fringe, which indicates that the stacking faults are intrinsic based on two-beam dynamical theory [30]. Thus the stacking fault structures formed in the matrix are similar in nature to those observed at smaller strain levels.

4. Discussion

4.1. Analysis of dislocation decorrelation

The concept of decorrelation of matrix dislocations due to interaction with precipitates has been discussed recently by Raujol et al. [31] and is based on their experimental observations in both turbine disk and turbine blade alloys. Moreover, the experimental evidence described above indicates that decorrelation of $a/2\langle 110\rangle$ matrix dislocations is a necessary precursor to microtwinning. While the possible

mechanisms for twin thickening will be discussed below, in this section we focus on developing a fundamental understanding of, and a predictive model for, the conditions for dislocation decorrelation.

4.1.1. Phase field simulation

In order to analyze all possible dislocation activities for a given γ channel width as a function of the orientation and magnitude of the in-plane shear stress phase field simulations of dislocation–precipitate interactions were carried out. Incorporating the generalized stacking fault (GSF) [32] energy of the octahedral slip plane, the phase field method [33,34] naturally describes dislocation dissociation and the associated stacking faults and partial dislocations in both the ordered and disordered phases. The results (Fig. 10) show that a rich variety of dislocation activities

can be observed, including Orowan looping and anti-phase boundary (APB) shearing by a full dislocation, Orowan looping by both partial dislocations, Orowan looping by only the leading partial, and stopping of both partials at the entrance to the γ' channel. Periodic boundary conditions create an array of spherical secondary γ' particles with a radius of 150 nm. The γ channel width between the γ' particles is 77.1 nm, as shown in the schematic drawing (lower right corner of Fig. 10). The Burgers vector direction for the perfect $a/2\langle 1 1 0\rangle$ dislocation is along the vertical direction (set as 0°), thus the Burgers vector for the leading partial $A\delta$ is along $+30°$ and the trailing partial δB is along $-30°$, as illustrated schematically in the center of Fig. 10. The angle θ between the in-plane shear stress direction and the Burgers vector direction of the perfect dislocation AB can vary from $-180°$ to $+180°$ (however,
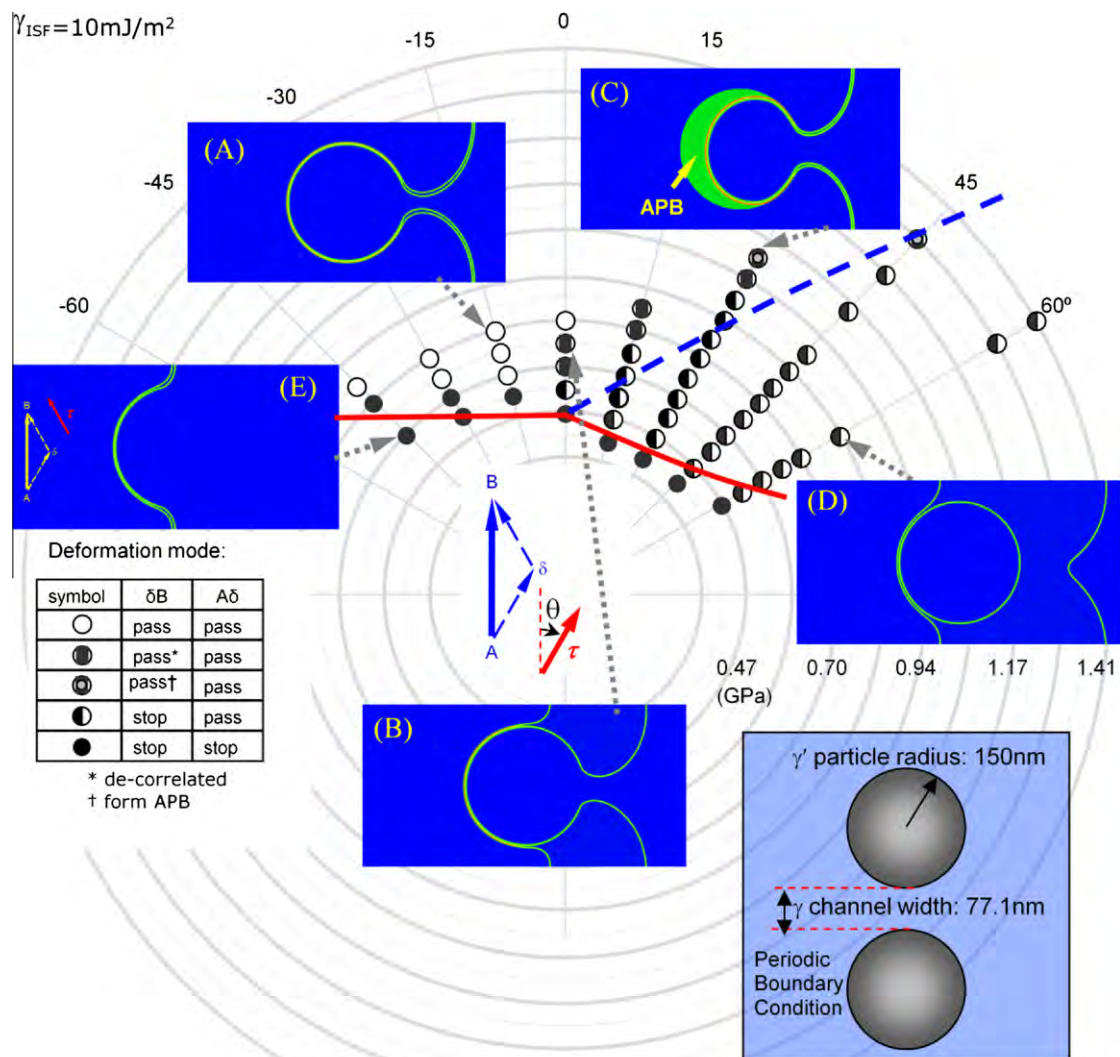
Fig. 10. Dislocation activity diagram comparing the analytical formulae with the phase field simulation results (lines are from the analytical formulae, symbols are calculated from phase field simulations). (A) Orowan bowing of full dislocation; (B) Orowan bowing of both partial dislocations (dislocation dissociation); (C) APB shearing of γ'; (D) Orowan bowing of the leading partial dislocation (decorrelation); (E) dislocations arrested in front of the channel. Note that the leading partial Burgers vector is $A\delta$, while that for the trailing partial is δB.

for $\theta > 90°$ or $\theta < -90°$, δB should be defined as the leading partial and the dislocation should initially be placed on the right side of the γ' particles). As indicated in the plot, each dot in Fig. 10 corresponds to one phase field simulation performed under that specific stress magnitude and orientation θ. Different symbols represent different dislocation activities, which are explained in the inset table in Fig. 10.

4.1.2. Analytical modeling

Based on the phase field simulation results, analytical expressions have been developed to determine the condition for $a/2\langle 1 1 0 \rangle$ dislocation dissociation as a function of the magnitude and orientation of the shear stress τ, the intrinsic stacking fault (ISF) energy γ^{ISF}, the friction force on partial dislocations τ_f due to solute drag or cutting of smaller tertiary γ' precipitates [35], and the influence of microstructure (γ channel width between secondary γ' particles). This development is based on the classical Orowan bowing mechanism [36]. For simplicity the dependence of the line tension on the screw/edge character of the dislocation (i.e. the angle between the dislocation sense vector and the Burgers vector) is ignored, thus the line tension is assumed to be $T = (\alpha\mu b^2)/2$, where α is a constant whose typical value is 1–2.

Depending on the orientation of the Burgers vector of the dislocation with respect to the applied stress, the leading Shockley partial could have a higher or lower resolved shear stress compared with the trailing one. In general, decorrelated motion of the partial dislocations can take place only if the leading partial has a higher resolved shear stress. Exceptions may exist considering the reduction in the effective channel width for the trailing partial to pass through when the leading one deposits segments in the channel, which repel the trailing one, especially for narrow γ channel widths and low ISF energy cases, which will be elaborated later.

The detailed formulation of the analytical model is presented in the Appendix A. According to the model the critical in-plane stress for the leading partial to bow through the channel τ_{crss}^t (which corresponds to the configuration shown in Fig. 11a) is expressed as:

$$\tau_{crss}^l = \frac{2\tau_f}{\cos(\theta_l) + \cos(\theta_t)} + \frac{\alpha\mu b}{\lambda\cos(\theta_l)}$$
$$\text{for } \cos(\theta_l) > \cos(\theta_t)$$
$$\tau_{crss}^l = \frac{2}{\cos(\theta_l) + \cos(\theta_t)}\left(\frac{\alpha\mu b}{\lambda} + \tau_f\right)$$
$$\text{for } \cos(\theta_l) \leqslant \cos(\theta_t) \qquad (1)$$

where θ_l is the angle between the applied stress and the Burgers vector of the leading partial and θ_t is the angle between the stress and the Burgers vector of the trailing partial. The channel width is λ and τ_f is the friction force caused by solute drag or the cutting of tertiary particles.

The force balance at the critical moment for the trailing partial dislocation to bow through the channel (which corresponds to the configuration shown in Fig. 11b) is:

$$\tau_{crss}^t \cos(\theta_t) = \tau_f + \frac{\alpha \cdot \mu b}{\lambda - 2H} - \frac{\gamma^{ISF}}{b} \qquad (2)$$

τ_{crss}^t is the corresponding critical stress for the trailing partial dislocation to pass through the channel, H is the distance between the deposited leading particle segments in the channel and the trailing dislocation, which is a function of τ_{crss}^t, and γ^{ISF} is the intrinsic stacking fault energy.

These analytical equations of the critical stresses are validated against the phase field simulation results. Materials parameters used in both the phase field simulations and the analytical formulae are as follows: $\{1 1 1\}$ plane shear modulus for both the γ and γ' phases is $\mu = 67.2$ GPa, the ISF energy is 10 mJ m^{-2}, and the dislocation line tension is $T = 2.45(\mu b^2/2)$. Note that the line tension chosen for these calculations is relatively high (i.e. $\alpha = 2.45$, which is higher than the typical α value of 1–2 as previously mentioned) because the extra gradient energy term in the phase field dislocation model at the length scale indicated in Fig. 10 leads to a relatively high line tension [37]. In order to make a quantitative comparison with the phase field simulation results the same line tension is used in the analytical model. In addition, the numerical grid in the phase field simulations effectively creates a friction force (Peierls stress) calibrated as $\tau_f = 100$ MPa and the same friction force is assumed in the analytical model as well. Considering the diffuse nature of dislocation cores in the phase field simulations at such a coarse grained length scale the channel width for the leading dislocation is 77.1 nm and that for the trailing one is 65.4 nm. The same channel widths are assumed in the analytical calculations.

The analytical result (solid red line and dashed blue line) is superimposed on the phase field simulation results in Fig. 10. The solid red[1] curve is the critical stress for the leading dislocation to pass through the channel and the dashed blue curve is the critical stress for the trailing dislocation to pass through. As observed, the analytical calculations agree reasonably well with the phase field simulations. The deviation of the critical stress for the leading partial at high θ angles is an artifact that will be discussed in the following section. As will be shown below, implementation of the analytical formulae allows a quick identification of the conditions (stress magnitude, orientation, intrinsic stacking fault energy, γ channel width, friction force, etc.) under which decorrelated motion of Shockley partials occurs for a given microstructure, as well as helps avoiding issues associated with coarse-graining to the length scale considered in this paper such as high dislocation line tension and high friction force.

4.1.3. Effect of applied stress on dislocation decorrelation

From the applied tensile stress in the experiment (724 MPa) the maximum in-plane shear stress is calculated as 362 MPa, which is indicated in Fig. 12 by the boundary

---

[1] For interpretation of color in Figs. 1, 4, 7, 10–14, the reader is referred to the web version of this article.

Fig. 11. Schematic illustrations depicting (a) the critical moment for the leading Shockley partial to pass through the channel and (b) the critical configuration for the trailing Shockley partial dislocation to pass through the γ channel.

Fig. 12. Critical stress plot (friction stress τ_f = 50 MPa, channel width 64 nm, γ^{ISF} = 10 mJ m^{-2}, line tension $T = (\mu b^2)/2$. The solid red line (marked L) is the critical stress for the leading partial calculated using the analytical form from Eq. (1); the solid blue line (marked T) is the critical stress for the trailing partial calculated using the solution of Eq. (2); the dotted red line (marked L′) is the critical stress for the leading partial calculated using a simplified form; the dotted blue line (marked T′) is the critical stress for the trailing partial calculated using a simplified form.

of the shaded area. The materials parameters used in the calculations were: elastic constants of the γ matrix, C_{11} = 224.3 GPa, C_{12} = 148.6 GPa, C_{44} = 125.8 GPa [38]; the corresponding shear modulus for the {1 1 1} slip plane $\mu = 67.2$ GPa; the Poison's ratio $v = \frac{C_{12}}{C_{11}+C_{12}} = 0.4$; the lattice constant of the γ matrix phase $a = 0.358$ nm; the Burgers vector of the Shockley partials $b = 0.146$ nm. The

friction force due to solute drag or shearing of tertiary particles is estimated to be 50 MPa [31]. Since this estimation was made for room temperature it is expected to be an upper bound of the friction force operative at the creep temperature of 677 °C. Although the experimental results indicate that the intrinsic stacking fault (ISF) energy γ^{ISF} is ∼25–30 mJ m^{-2} at intermediate temperatures [39], a

more recent quantitative analysis of the Shockley partial dissociation suggests that $\gamma^{\mathrm{ISF}} \approx 10 \text{ mJ m}^{-2}$ [31]. Thus $\gamma^{\mathrm{ISF}} = 10 \text{ mJ m}^{-2}$ was chosen for the calculations. For simplicity the line tension was assumed to be $T = (\mu b^2/2)$ regardless of its character (edge or screw). Fig. 12 shows the calculation results obtained for a γ channel width of 64 nm, which corresponds well with the average channel width measured experimentally. The red curve (marked L) is the critical stress for the leading partial to pass through the channel, while the blue curve (marked T) is the critical stress for the trailing partial to pass through. It can be seen from Fig. 12 that when the resolved shear stress on the leading partial becomes smaller than that on the trailing one ($\theta < 0$) the two curves collapse, indicating no decorrelated motion.

For a shear stress level of 362 MPa, as long as the angle θ between the shear stress direction and the full dislocation Burgers vector direction is between $+70°$ and $+33°$, decorrelated motion of partials is expected because the leading partial can go through the 64 nm channel while the trailing partial cannot. For angles from $+33°$ to the branching point of the curve (marked X on the plot, around $+9°$) both dislocations can go through the channel, although the leading one still has a higher resolved stress, which means it moves faster than the trailing one. In this case decorrelated motion is still possible, but depends on the difference between the critical stress for the leading and trailing partials. For θ between $+9°$ to $-53°$ the partials will pass through the channel together as the trailing one pushes the leading one, and thus no decorrelated motion will occur and shearing by perfect $a/2\langle 1 1 0 \rangle$ dislocations should dominate the deformation process. For θ between $-53°$ and $-90°$ no dislocation is able to pass through the channel at this stress level.

The decorrelation diagram with respect to stress orientation has mirror symmetry relative to the normal of the $a/2\langle 1 1 0 \rangle$ full Burgers vector (the dislocation will move from the right to the left in this case, because of reversal of the in-plane shear stress orientation). Hence, there will be large asymmetry for a given slip vector depending upon the sign of the applied shear stress. This asymmetry is brought about by the reversed role of the leading and trailing Shockley partials. Moreover, for a $\{1 1 1\}$ slip plane there are three co-planar $a/2\langle 1 1 0 \rangle$ dislocations, AB, BC, and AC, whose Burgers vectors are 120° apart. By considering the dissociation of all three types of full dislocations the probability of observing decorrelated dislocation motion for a random orientated 362 MPa in-plane shear stress is about 78% for an average channel width of 64 nm.

Douin et al. [40] also proposed a set of simple analytical forms to describe the dissociation process that provides the critical stress of the leading, trailing, and full dislocations. The results are plotted in Fig. 12 (incorporating the additional solute drag friction stress τ_f) as dashed lines (the line for leading dislocation is marked L′, the line for trailing dislocation is marked T′, and the line for full dislocation is marked S, within the $-90° < \theta \leqslant 90°$ region). Clear dis-

agreements exist between the two calculation results. Compared with Eq. (1) the critical stress calculated for line L′ does not take into account the assistance from the trailing dislocation through elastic interaction. Thus Eq. (1) gives a lower critical stress when $\theta \leqslant 60°$. However, when $\theta > 60°$ (for $-90° < \theta \leqslant 90°$, when $A\delta$ is still defined as the "leading partial") the resolved shear stress on the trailing partial δB becomes negative, which means that δB is driven to move in the opposite direction with respect to $A\delta$. In this case the scenario shown in Fig. 11a is no longer accurate because the trailing partial tends to move away from the leading partial. Under this condition the critical stress calculated for line L′, which is established for large separation distances between the partials, can better describe the critical stress for the leading partial. As for the trailing dislocation, the critical stress calculated for line T′ does not take into account the reduction in effective channel width due to the segments laid by the leading partial, which in turn underestimates the critical stress level.

4.1.4. Effect of microstructure on dislocation dissociation and microtwinning

Previous work has shown that for deformation conditions that produce microtwins in the finer scale precipitate microstructure considered in this work a different deformation mode appears to be dominant for a coarser precipitate microstructure developed by a slower cooling rate from the supersolvus temperature [41]. For this latter microstructure, which simulates that in the "bore" region of a turbine disk, deformation occurs by intense $a/2\langle 1 1 0 \rangle$ dislocation activity in the matrix, with occasional shearing of the precipitates by superlattice intrinsic or extrinsic stacking faults. Thus for this coarser microstructure dislocation decorrelation does not seem to occur. Rather, matrix perfect dislocations seem to retain their ability to percolate through the γ channels. The analytical model developed above provides an insight into this microstructure effect.

In Fig. 13 the average channel width is assumed to be 159 nm, which corresponds to the microstructure observed in the bore region. As expected, the wider channel makes it easier for dislocations to pass through, and the critical stress level decreases. When compared with Fig. 12, it can also be observed that the intersection of the critical stress for the trailing dislocation to pass through the channel with the 362 MPa applied shear stress contour is shifted from $+33°$ to $+50°$ as the channel width increases. Thus, decorrelation of partials is less likely (in terms of the angular range of the shear stress). Considering all three co-planar $a/2\langle 1 1 0 \rangle$ dislocations, the probability of observing decorrelated dislocation motion for a randomly oriented in-plane shear stress of 362 MPa is 51% for a channel width of 159 nm, compared with 78% for a channel width of 64 nm, considered earlier. (Note that the probabilities considered here are for decorrelation of any of the three co-planar slip systems under a randomly oriented 362 MPa in-plane shear stress.) Thus, depending on the applied stress, there will be a certain range of channel widths that maximize the probability of
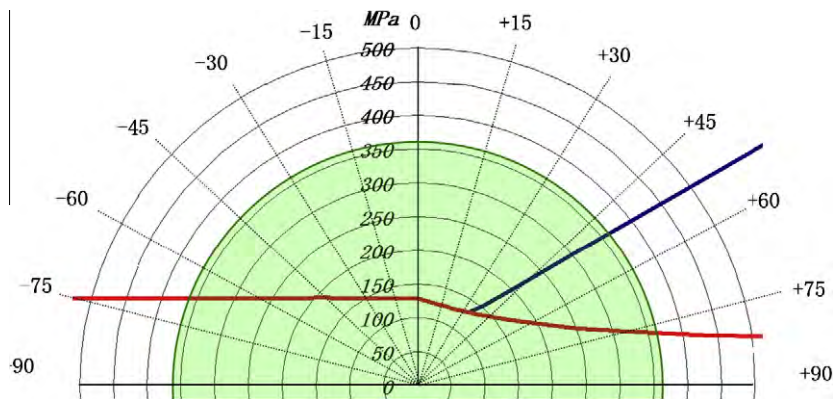
Fig. 13. Critical stress plot (friction stress τ_f = 50 MPa, channel width 159 nm, γ^{ISF} = 10 mJ m^{-2}, α = 1, line tension T = (μb^2)/2. The solid red line is the critical stress for the leading partial calculated using the analytical form from Eq. (1); the solid blue line is the critical stress for the trailing partial calculated using the solution of Eq. (2).

decorrelated dislocation motion. For instance, if the in-plane stress is 200 MPa instead of 362 MPa, then for a channel width of 64 nm even the leading partial dislocation cannot pass though. For a channel width of 159 nm dissociation is still possible. Using these analytical formulae we may identify the optimal stress level for a given microstructure, or specify target microstructures for a given applied stress, that will favor matrix dislocations or microtwinning as the dominant deformation mode.

4.2. Transition from stacking faults to microtwins

A comprehensive review of deformation twinning has been provided by Christian and Mahajan [19]. Possibilities for the creation of microtwins from intrinsic matrix stacking fault structures have been identified. The pole mechanism has been proposed to describe twinning in fcc crystals [42]. In this model it is envisioned that a twin is formed from a perfect $a/2\langle 110\rangle$ dislocation that acts as an anchor point where the twinning dislocation ($a/6\langle 112\rangle$ Shockley partial) sweeps out on {1 1 1} glide planes and rotates about the pole to produce the twin. Alternatively, in the model proposed by Mahajan and Chin [43] two co-planar $a/2\langle 110\rangle$ dislocations with different Burgers vectors are envisioned to react and form three identical Shockley partial dislocations on adjacent {1 1 1} glide planes, thereby acting as the nucleus of a three layer twin. From the limited experimental evidence of microtwinning in polycrystalline γ' strengthened superalloys investigated recently [14–16] it appears that all of the $a/2\langle 110\rangle$ dislocations that are observed to dissociate into Shockley partial dislocations have the same Burgers vector. Accordingly, these observations suggest that the microtwinning mechanism in these alloys differs from that proposed by Mahajan and Chin. Furthermore, in the double cross-slip model proposed by Pirouz a single screw oriented $a/2\langle 110\rangle$ dislocation dissociates into two Shockley partial dislocations [44]. Similarly to a Frank–Read source, the large shear stress imposed on the leading Shockley partial dislocation will bow out and create an intrinsic stacking fault. As the

leading Shockley partial recombines with the static, trailing partial the $a/2\langle 110\rangle$ dislocation that is once again created can cross-slip (along its screw orientation) to an adjacent {1 1 1} plane, then redissociate into Shockley partial dislocations in the same manner as the dissociation on the initial {1 1 1} plane. If this operation were to be repeated on multiple adjacent {1 1 1} planes then Shockley partial dislocations possessing the same Burgers vector would be operative, and a microtwin could potentially develop. Based on the present work it is impossible to definitively validate this mechanism, however, it is noted that this mechanism is consistent with the operation of single $a/2\langle 110\rangle$ slip systems as the source of the twins.

The present observation, that extended intrinsic faults form in the γ matrix preceding the onset of microtwinning, brings to bear another possibility for microtwin formation. It has been shown that these intrinsic faults form from the dissociation of $a/2\langle 110\rangle$ dislocations that originate near intragranular carbides and intergranular carbides/borides. Under appropriate shear stress conditions the matrix dislocations undergo decorrelation, with the leading partial dislocation percolating between the secondary γ' particles and laying out large areas of intrinsic stacking faults. With these intrinsic stacking faults established, the subsequent interaction of another matrix dislocation will create a scenario such as that illustrated in Fig. 14. Here it is envisioned that the same $a/2\langle 110\rangle$ dislocation type cross-slips onto the intrinsic stacking fault plane, then dissociates. As the leading partial of this second dislocation drives forward it creates an extrinsic stacking fault in the matrix. As this partial reaches locations where the first leading partial has been arrested at γ' particles, the pair of identical Shockley partials are then able to traverse γ' via reorder-mediated shearing [22]. This process will result in the removal of the Shockley partial loops surrounding the γ' particles, as observed for instance in Fig. 7, and the creation of SESF in the sheared γ' particles following reordering. Repetition of this process of matrix dislocation cross-slip, extension, and reorder-mediated shearing would enable thickening of the extrinsic stacking faults/SESF into multilayer
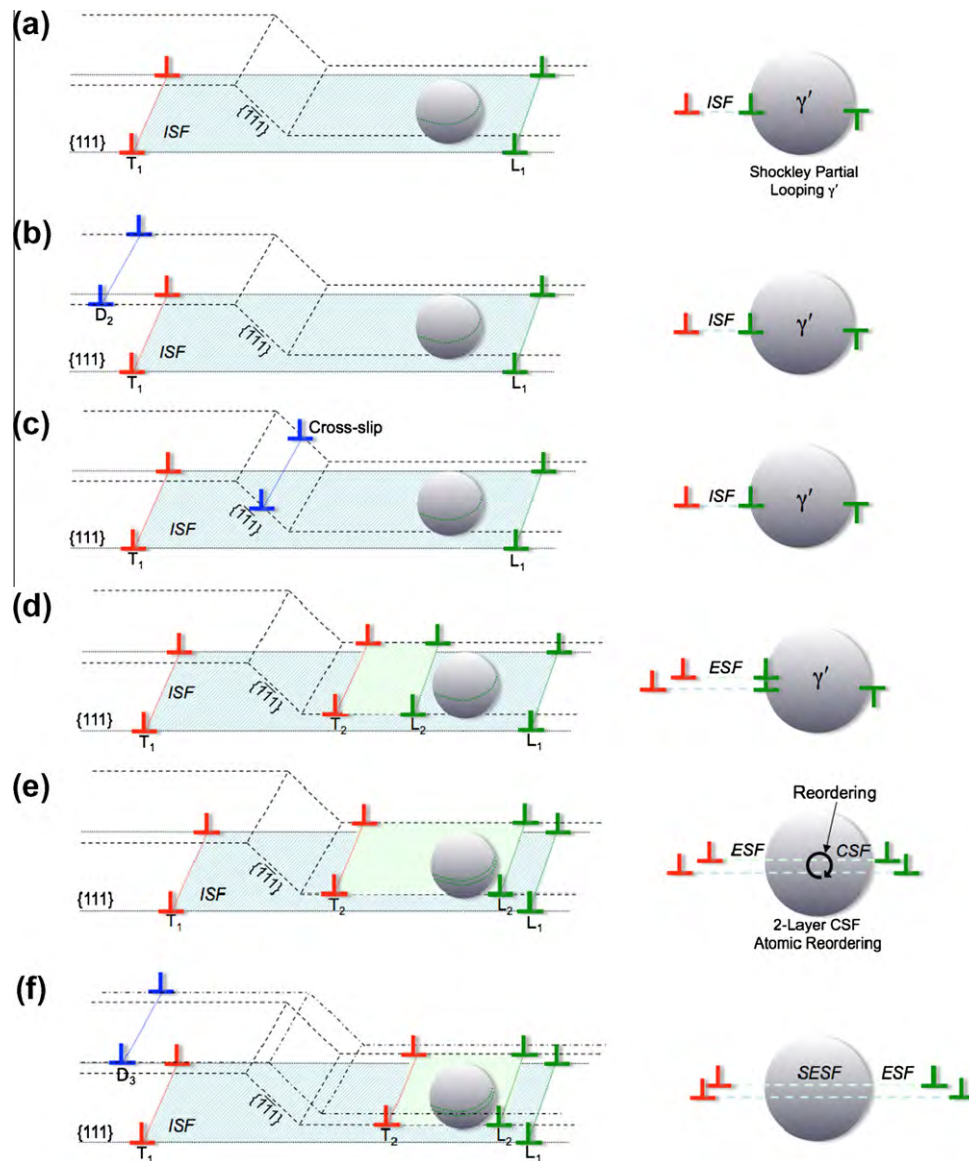
Fig. 14. Possible scenario for transition from dissociated $a/2\langle110\rangle$ type dislocations and decorrelated leading (L_1) and trailing (T_1) Shockley partial bounding matrix stacking faults into microtwins through a sequence of cross-slip and dissociation steps of subsequent $a/2\langle110\rangle$ dislocations. After γ' is (a) looped by the leading Shockley partial, the key steps are (b and c) the approach and cross-slip of a second $a/2\langle110\rangle$ dislocation, (d) dissociation of the second $a/2\langle110\rangle$ dislocation (D_2) on the {111} plane adjacent to the stacking fault, (e) cooperative shearing of γ' by two Shockley partials by reorder-mediated motion, creating superlattice extrinsic stacking in γ' and an extrinsic stacking fault in the matrix, (f) approach of a third $a/2\langle110\rangle$ dislocation (D_3). Repetition of this process would enable thickening into microtwins.

microtwins. This scenario is also consistent with the observation of microtwins in the absence of significant secondary slip system activity [45]. Clearly, the trailing Shockley partials that do not participate in the forward shearing process would accumulate near the origin of the twins. Their mutual stress fields could eventually inhibit further thickening of the microtwins by this cross-slip process. This may provide an explanation for the predominance of thin microtwins, with few as thick as that shown in Fig. 4c.

5. Conclusions

Through a detailed TEM characterization study on the early stages of creep deformation in a γ' strengthened Ni-based superalloy it was possible to identify discrete locations where deformation microtwins may have nucleated. Microtwinning is an important creep deformation mode at low stress and intermediate temperatures (650–750 °C). It was found that carbides and borides, which are either situated at the grain boundaries or within the grain interiors, acted as sources for $a/2\langle110\rangle$ matrix dislocations. At small strain levels matrix dislocations are frequently observed to dissociate (i.e. decorrelate) into Shockley partial dislocations, creating broad intrinsic stacking faults in the γ matrix. Under similar creep conditions but larger strain levels microtwinning is observed to dominate the deformation. Thus matrix dislocation decorrelation appears to be a key precursor to microtwinning.

The decorrelation process is driven by the relative forces acting on the two Shockley partial dislocations of a perfect $a/2\langle 110\rangle$ -type matrix dislocation in the narrow confines of the γ matrix channels, since the γ precipitates cannot be sheared by the leading Shockley partials. A detailed analysis of these forces has been performed using computer simulations based on a phase field dislocation model, upon which an analytical model was also developed. In the analysis a consistent picture emerges demonstrating the possibility of a rich variety of behaviors depending on several factors, including orientation of the applied shear stress relative to the dislocation Burgers vectors, the γ channel width, and the matrix stacking fault energy. The models predict that decorrelation can occur at low stress levels relative to other possible processes (such as Orowan bowing around particles) when the applied shear stress is suitably oriented so as to create a larger force on the leading Shockley partial dislocation. This result provides a natural explanation for the observation of matrix stacking faults dominating the substructure of many grains at small strain levels. Several possible scenarios for the subsequent thickening from intrinsic stacking faults into microtwins have also been discussed, including repeated cross-slip and dissociation of matrix dislocations onto pre-existing stacking faults.

Appendix A. Analytical model of dislocation dissociation

During the critical moment when the leading partial is attempting to bow through a γ channel between two γ' particles, as indicated in Fig. 11a, the resolved shear stress on the leading partial is $\tau\cos(\theta_l)$ and that on the trailing partial is $\tau\cos(\theta_t)$, where θ_l is the angle between the applied stress and the Burgers vector of the leading partial and θ_t is the angle between the stress and the Burgers vector of the trailing partial, as shown in Fig. 12. If the angle between the stress and the Burgers vector of the full dislocation is θ, then $\theta_t = 30° + \theta$ and $\theta_l = 30° - \theta$.

The leading partial experiences a repulsion force f^d from the elastic interaction with the trailing partial and a drag from the intrinsic stacking fault between them. According to the Orowan equation [36] the critical resolved shear

stress on the leading particle τ_{crss}^l for passage through the γ channel between two γ' particles is given by the equation:

$$\frac{f^d}{b} + \tau_{crss}^l \cos(\theta_l) - \tau_f = \frac{\alpha \cdot \mu b}{\lambda} \tag{A1}$$

where λ is the channel width. Assuming that the trailing segment close to the channel has a local curvature of r_t (see arrow in Fig. 11a), the force balance on the trailing one is:

$$\tau_{crss}^l \cos(\theta_t) - \tau_f - \frac{\alpha \cdot \mu b}{2r_t} = \frac{f^d}{b} \tag{A2}$$

The local curvature of the trailing partial at this critical moment can be estimated if we assume that the resolved shear stress is much greater than the friction force, i.e.

$$\frac{\tau_{crss}^l}{\alpha \cdot \mu b} \approx \frac{1}{\cos(\theta_l)}\frac{1}{\lambda} = \frac{1}{\cos(\theta_l)}\frac{1}{2r_t} \tag{A3}$$

Thus

$$2r_t = \lambda\frac{\cos(\theta_l)}{\cos(\theta_t)} \tag{A4}$$

when $\cos(\theta_l) > \cos(\theta_t)$. When $\cos(\theta_l) \leqslant \cos(\theta_t)$ the resolved shear stress on the leading partial is lower than or equal to that on the trailing one and hence the trailing partial will push the leading one. In this case the two dislocations will have similar curvatures at the critical moment (indicated in Fig. 11a by the dotted line for the trailing dislocation), i.e.

$$2r_t \approx \lambda \tag{A5}$$

When r_t is known the critical in-plane stress for the leading partial to bow through the channel is:

$$\tau_{crss}^l = \frac{2\tau_f}{\cos(\theta_l) + \cos(\theta_t)} + \frac{\alpha\mu b}{\lambda\cos(\theta_l)}$$

for $\cos(\theta_l) > \cos(\theta_t)$

$$\tau_{crss}^l = \frac{2}{\cos(\theta_l) + \cos(\theta_t)}\left(\frac{\alpha\mu b}{\lambda} + \tau_f\right)$$

for $\cos(\theta_l) \leqslant \cos(\theta_t)$ \tag{A6}

When the trailing dislocation attempts to pass through the channel, no matter whether the leading one has already passed through or is just moving together with and right in front of the trailing one when $\cos(\theta_l) \leqslant \cos(\theta_t)$, the leading partial must have already laid two segments at the γ/γ' interface inside the channel as illustrated in Fig. 11b. Thus the effective width of the channel is reduced for the trailing one due to the repulsive force of the deposited segments of the leading partial. The distance H between the deposited leading particle segments in the channel and the trailing dislocation can be calculated using the equation:

$$\tau_{crss}^t \cos(\theta_t)b + \gamma^{ISF} = \frac{\mu b^2}{4\pi H(1-\nu)} \tag{A7}$$

which represents the force balance between the resolved shear stress, the attractive force from the intrinsic stacking

fault and the repulsive force from the leading partial segment. τ_{crss}^t is the critical resolved shear stress for the trailing partial to pass through and v is the Poisson's ratio.

Considering that the effective channel width for the trailing partial is reduced to $\lambda - 2H$, the force balance at the critical moment for the trailing partial to bow through the channel is:

$$\tau_{crss}^t \cos(\theta_t) = \tau_f + \frac{\alpha \cdot \mu b}{\lambda - 2H} - \frac{\gamma^{ISF}}{b} \quad (A8)$$

As this is a quadratic function of τ_{crss}^t (note that H is a function of τ_{crss}^t) an analytical solution can be easily obtained. The other condition required for decorrelated motion is that $\tau_{crss}^t \geq \tau_{crss}^l$. If $\tau_{crss}^t < \tau_{crss}^l$ the trailing partial will push the leading one passing through the channel more or less simultaneously and thus there is no decorrelated motion.

References

[1] Pollock TM, Argon AS. Acta Metall Mater 1992;42(1):1.
[2] Levarant GR, Kear BH. Metall Trans 1970;1(2):491.
[3] Kear BH, Oblak JM, Giamei AF. Metall Trans 1970;1(9):2477.
[4] Link T, Feller-Kniepmeier M. Metall Trans 1992;23A:99.
[5] Rae CMF, Reed RC. Acta Mater 2007;55(3):1067.
[6] Caron P, Khan T, Veyssiere P. Philos Mag A 1988;57:859.
[7] Decamps B, Morton AJ, Condat M. Philos Mag A 1991;64:641.
[8] Bonnet R, Ati A. Scripta Metall Mater 1991;25:1553.
[9] Guimier A, Strudel JL. In: Proceedings of the 2nd international conference on the strength of metals and alloys, vol. 3; 1970. p. 1145.
[10] Ardakani MG, McLean M, Shollock BA. Acta Mater 1999;47(9):2593.
[11] Knowles DM, Gunturi S. Mater Sci Eng A 2002;328:223.
[12] Knowles DM, Chen QZ. Mater Sci Eng A 2003;340:88.
[13] Kakehi K. Scripta Mater 1999;41(5):461.
[14] Viswanathan GB, Sarosi PM, Henry MF, Whitis DD, Milligan WW, Mills MJ. Acta Mater 2005;53:3041.
[15] Viswanathan GB, Karthikeyan S, Sarosi PM, Unocic RR, Mills MJ. Philos Mag 2006;86(29–31):4823.
[16] Unocic RR, Viswanathan GB, Sarosi PM, Karthikeyan S, Li J, Mills MJ. Mater Sci Eng A 2008;483/484:25.
[17] Legros M, Clement N, Caron P, Coujou A. Mater Sci Eng A 2002;337:160.
[18] Honeycombe RWK. The plastic deformation of metals. London: Edward Arnold; 1984.
[19] Christian JW, Mahajan S. Prog Mater Sci 1995;39(1/2):1.
[20] Kolbe M. Mater Sci Eng A 2001;319:383.
[21] Karthikeyan S, Unocic RR, Sarosi PM, Viswanathan GB, Whitis DD, Mills MJ. Scripta Mater 2006;54(6):1157.
[22] Kovarik L, Unocic RR, Li J, Sarosi PM, Shen C, Wang Y, et al. Prog Mater Sci 2009;54(6):839.
[23] Zhou N, Shen C, Mills MJ, Li J, Wang Y. Acta Mater 2011;59(9):3484.
[24] Mourer DP, Williams JL. In: Green KA, Pollock TM, Harada H, Howson TE, Reed RC, Schirra JJ, editors. 10th International symposium on superalloys, Champion, PA; 2004. p. 401.
[25] Sarosi PM, Wang B, Simmons JP, Wang Y, Mills MJ. Scripta Mater. 2007;57:767.
[26] Wlodek ST, Kelly M, Alden DA. In: Kissinger RD, Deye DJ, Anton DL, Cetel AD, Nathal MV, Pollock, et al., editors. 8th International symposium on superalloys, Champion, PA; 1996. p. 129.
[27] Sarosi PM, Viswanathan GB, Mills MJ. Scripta Mater 2006;55:727.
[28] Wlodek ST. In: Fuchs GE, Dannemann KA, Deragon TA, editors. Long term stability of high temperature materials. Warrendale (PA): TMS; 1999. p. 3.
[29] Donachie MJ, Donachie SJ. Superalloys: a technical guide. Materials Park (OH): ASM International; 2002.
[30] Williams DB, Carter CB. Transmission electron microscopy. New York: Plenum Press; 1996. p. 381.
[31] Raujol S, Benyoucef M, Locq D, Caron P, Pettinari F, Clement N, et al. Philos Mag 2006;86(9):1189.
[32] Vitek V. Philos Mag 1968;18(154):773.
[33] Shen C, Wang Y. Acta Mater 2003;51(9):2595.
[34] Shen C, Wang Y. Acta Mater 2004;52(3):683.
[35] Jouiad M, Pettinari E, Clement N, Coujou A. Philos Mag 1999;79(11):2591.
[36] Orowan E, Zeits F. Physik 1934;89:605–59.
[37] Wang YU, Jin TM, Cuitino AM, Khachturyan AG. Acta Mater 2001;49(10):1847.
[38] Kayser FX, Stassis C. Phys Stat Sol 1981;64(1):335.
[39] Pettinari F, Douin J, Saada G, Caron P, Coujou A, Clement N. Mater Sci Eng 2002;325:511.
[40] Douin J, Pettinari-Sturmel F, Coujou A. Acta Mater 2007;55:6453.
[41] Unocic RR, Kovarik L, Shen C, Sarosi PM, Wang Y, Li J, et al. In: Reed RC, Green KA, Gabb TP, Fahrmann MG, Huron ES, editors. 11th International symposium on superalloys, Champion, PA; 2008. p. 377.
[42] Venables JA. Philos Mag 1961;6:379.
[43] Mahajan S, Chin GY. Acta Metall 1973;21:1353.
[44] Pirouz P. Scripta Metall 1987;21:1463.
[45] Unocic RR. PhD dissertation. The Ohio State University; 2008.